Electrode-Shaping for the Excitation and Detection of Permitted Arbitrary Modes in Arbitrary Geometries in Piezoelectric Resonators

Jeffrey S. Pulskamp, Sarah S. Bedair, *Member, IEEE*, Ronald G. Polcawich, *Member, IEEE*, Gabriel L. Smith, Joel Martin, Brian Power, and Sunil A. Bhave

Abstract—This paper reports theoretical analysis and experimental results on a numerical electrode shaping design technique that permits the excitation of arbitrary modes in arbitrary geometries for piezoelectric resonators, for those modes permitted to exist by the nonzero piezoelectric coefficients and electrode configuration. The technique directly determines optimal electrode shapes by assessing the local suitability of excitation and detection electrode placement on two-port resonators without the need for iterative numerical techniques. The technique is demonstrated in 61 different electrode designs in lead zirconate titanate (PZT) thin film on silicon RF micro electro-mechanical system (MEMS) plate, beam, ring, and disc resonators for out-of-plane flexural and various contour modes up to 200 MHz. The average squared effective electromechanical coupling factor for the designs was 0.54%, approximately equivalent to the theoretical maximum value of 0.53% for a fully electroded length-extensional mode beam resonator comprised of the same composite. The average improvement in S_{21} for the electrode-shaped designs was 14.6 dB with a maximum improvement of 44.3 dB. Through this piezoelectric electrode-shaping technique, 95% of the designs showed a reduction in insertion loss.

I. INTRODUCTION

CONSUMER electronics industries continue to demand greater levels of integration of radio frequency selective and frequency reference devices. Size limitations and large scale-integration challenges of quartz and SAW devices will limit their application in future systems. Conversely, the success of thin-film bulk acoustic resonators (FBAR) can be attributed to their relative ease of integration, small scale, gigahertz frequency operation, and strong electromechanical coupling [1], [2]. However, the reliance on film thickness to set frequency in the thickness-mode vibrations of FBARs poses significant challenges to achieving compact integration of multiple frequencies on the same chip.

Micro electro-mechanical system (MEMS)-based electromechanical resonators have received significant atten-

tion over the past two decades for their potential to provide highly integrated, low-power, and small form factor solutions for multiband devices [3], [4]. The use of contour and other vibrational modes, for which the frequency setting dimensions are largely determined by the in-plane lithographically defined dimensions, enables MEMS resonators to address the chief limitation of FBARs. MEMS resonators, filters, and oscillators are now achieving motional resistances and quality factors that are competitive with or superior to the current commercial solutions [5]–[7].

The drive to commercialize MEMS resonator technologies has led to a research focus on minimizing motional resistances and maximizing quality factors. In addition to achieving further improvements in these metrics, there remains a need to improve the suppression of spurious vibrational modes, increase resonant frequencies, improve power handling and linearity, and achieve wider bandwidth resonators for band-select filter applications. The existence of spurious modes can degrade the out-of-band rejection in filters, lead to unstable frequency operation in oscillators, and reduce the quality factor of desired modes. The use of high-frequency modes or high-order harmonics can increase operating frequencies without the need to continually reduce the resonator dimensions. The use of high-order harmonics can improve power handling by preserving a large resonator volume for a given operating frequency. In piezoelectric devices, stronger electromechanical coupling and, hence, wider filter bandwidths can be achieved by utilizing more favorable quasi-static material coupling factors [8].

The proper design of the resonator electrodes to selectively excite and detect desired modes, or electrode-shaping, can provide improvements in the aforementioned performance metrics. The recent use of high-order harmonics in extensional-mode piezoelectric MEMS resonators has led to the lowest motional resistances yet demonstrated in MEMS [6], [7]. These devices essentially place n fundamental mode resonators in parallel to reduce the motional resistance roughly by a factor of n, where n is the order of the harmonic [9]. An electrode-shaping technique that can accommodate arbitrary geometries and modes can further exploit this approach to minimizing motional resistance. These extensional modes generally utilize the piezoelectric k_{31}^2 coupling factor [10], which is among the weakest cou-

pling factors in thin film piezoelectrics. Electrode-shaping can permit the use of modes in geometries that exploit stronger coupling factors, such as the planar coupling factor k_p^2 to further reduce motional resistance and realize wider bandwidth filters. In addition, electrode-shaping can allow the use of vibrational modes in geometries that have large nodal regions of low strain energy that facilitate resonator support design to minimize anchor loss or permit larger tether geometries with correspondingly reduced resistive and reactive parasitics.

The first demonstration of electrode-shaping to achieve the desired input-output characteristics of transducers, or "modal actuators and sensors," was described in 1990 by Lee and Moon [11]. Ideally, modal transducers only excite or detect a single desired frequency in the structural response of the system. There has been an extensive body of research on modal transducers since that time, particularly for applications in active vibration control of structures [12]–[16]. Irschik *et al.* present a good review of piezoelectric modal transducers in [17]. Formal optimization approaches have also been applied to the shaping problem; a review may be found in [18]. In particular, several researchers have successfully applied topology optimization techniques to the design of piezoelectric smart structures [19]–[23].

Many vibrational modes have been utilized for MEMS resonator devices; including the flexural vibrations of clamped-clamped and free-free beams, the extensional contour modes of beams, discs, and rings, and thickness extensional vibrations in FBARs [24]–[30]. However, the excitation and detection electrodes are designed for specific structures and specific modes in the absence of a general technique to assess arbitrary cases. In the early 1990s, Prak *et al.* [31] and Tilmans *et al.* [32] demonstrated the principle of electrode-shaping for the selective excitation and detection of one-dimensional vibrational modes in MEMS resonators. More recently, Elka *et al.* applied the concepts of modal filters with a Lyapunov equation-based optimization approach to design electrodes for electrostatically transduced one-dimensional modes in free-free MEMS resonators [33]. Recently, Sanchez-Rojas *et al.* applied a topology optimization scheme to the design of piezoelectric low-frequency MEMS plate resonators [34]. The electrode-shaping theory utilized was developed in [35] and is limited to the description of out-of-plane flexure modes in plates.

Experimentally verifying that an electrode-shaped resonator design successfully achieves selective excitation and detection of the desired mode has posed certain challenges. Fundamentally, such an experiment must provide a relative measure of selective excitation and detection; the mere measured presence or absence of a mode does not establish the viability of the design technique. In addition, various responses can be measured to assess excitation and detection; mechanical displacement or high-frequency electrical response, for example. Prior works [31], [34] have utilized low-frequency mechanical displacement frequency

response measurements of a few example devices to assess electrode shaping. For RF MEMS applications, electromechanical coupling factors and scattering parameters are more suitable measures of excitation and detection. For techniques capable of handling arbitrary cases of geometry and mode, it is also desirable to obtain statistically significant measurements across a diverse set of examples.

The vast majority of the prior work in modal transducers and electrode shaped piezoelectric devices has been limited to the treatment of simple one-dimensional modes. The techniques developed to treat higher dimensional modes have either addressed very simple cases or have required non-intuitive iterative approaches such as topology optimization. In contrast, this article presents an advanced modeling and design technique that permits the piezoelectric excitation and detection of vibrational modes, for the first time, in arbitrary cases for those modes permitted to exist by the nonzero piezoelectric coefficients and electrode configuration. The technique directly solves for the electrode shapes without the need for numerical iteration. The technique determines optimal electrode shapes, with respect to force and charge cancellation over the electroded surface, that permit the excitation and detection of the desired mode. This represents a key step toward realizing an electrode shaping technique for the design of piezoelectric modal transducers for arbitrary cases of geometry and mode.

II. Theory

For resonator applications, electrode shaping can be utilized to ensure the desired mode is excited and/or detected, and furthermore to maximally suppress undesired modes or maximally excite and/or detect the desired mode. The essential feature of electrode shaping is to avoid cancellation of distributed forces at the excitation port and charges or current at the detection port. Before describing the numerical approach, it is useful to review the one-dimensional analytical theory.

A. Analytical Example

The first step in electrode-shaping is assessing modal excitation based on the distribution of the driving loads. Modal analysis is a useful and common approach to modeling the frequency response of structures and provides the basis for modeling modal excitation [36]. The key advantage of modal analysis is that it decouples the equation of motion of multiple degree-of-freedom systems via the orthogonality property of the mode shapes; it linearly transforms the coupled second-order differential equations of motion to a series of decoupled differential equations [37], [38]. This allows the treatment of an isolated mode of a continuous structure as a single-degree-of-freedom system with lumped element properties.

The shape of the mode shapes are unique but their magnitudes are not. Hence, the mode shapes are common-

ly normalized to render them unique [37]. For example, consider the length-extensional mode of a free-free beam. For this one-dimensional mode, we may normalize the mode shapes by utilizing the common mass normalization scheme such that the mode shapes $\phi(x)$ satisfy the following orthogonality condition:

$$\int_0^L m(x)\phi_i(x)\phi_j(x)\mathrm{d}x = \delta_{ij}, \tag{1}$$

where L is the length of the beam, $m(x)$ is the distribution of the mass per unit length of the resonator, $\phi_i(x)$ is the mode shape of the ith mode, $\phi_j(x)$ is the mode shape of the jth mode, and δ_{ij} is the Kronecker delta [37]. Modal analysis describes the vibrational response as a linear combination of the modes such that the displacement response can be expressed as

$$y(x,t) = \sum_{i=1}^{\infty} \phi_i(x)\eta_i(t), \tag{2}$$

where $y(x,t)$ is the axial displacement of the resonator at location x and at time t and $\eta_i(t)$ is the modal (generalized) coordinate of the ith mode. The undamped equation of motion transformed into the modal coordinates yields the independent modal equations

$$\ddot{\eta}_i(t) + \omega_i^2\eta_i(t) = N_i(t), \tag{3}$$

where ω_i is the resonant frequency and $N_i(t)$ is the modal force of the ith mode, respectively. For the case of a harmonic excitation force, the modal force can be described by

$$N_i(t) = \left[\int_0^L \varphi_i(x)\frac{F_{\mathrm{app}}(x)}{L}\mathrm{d}x\right]\cos\Omega t = F_i\cos\Omega t, \tag{4}$$

where $F_{\mathrm{app}}(x)$ is the distribution of the externally applied excitation loads, Ω is the excitation frequency, and F_i is the amplitude of the ith modal force, defined by

$$F_i = \int_0^L \phi_i(x)\frac{F_{\mathrm{app}}(x)}{L}\mathrm{d}x. \tag{5}$$

Inserting (4) into (3), the steady-state solution of (3) for the modal coordinate yields

$$\eta_i(t) = \frac{F_i}{\omega_i^2 - \Omega^2}\cos\Omega t \tag{6}$$

Inserting (5) and (6) into (2) yields the steady-state displacement response under harmonic excitation:

$$y(x,t) = \left[\sum_{i=1}^{\infty} \frac{\int_0^L \phi_i(x)\frac{F_{\mathrm{app}}(x)}{L}\mathrm{d}x}{\omega_i^2 - \Omega^2}\phi_i(x)\right]\cos\Omega t. \tag{7}$$

As discussed in [33] and [37], only modes with nonzero F_i will be excited. Furthermore, we can express (7) for the case in which F_j for the jth mode is chosen to be proportional to the product of $m(x)$ and $\phi_j(x)$ as

$$y(x,t) = \left[\sum_{i=1}^{\infty} \frac{C}{L}\frac{\phi_i(x)}{\omega_i^2 - \Omega^2}\left(\int_0^L m(x)\phi_i(x)\phi_j(x)\mathrm{d}x\right)\right]\cos\Omega t, \tag{8}$$

where C is a constant dependent upon the excitation magnitude. From the definition of the normalization scheme (1), it is clear that the integral within the parentheses in (8) is zero for all modes other than the jth mode. Therefore, the jth mode may be excited exclusively if Fj is proportional to the product of $m(x)$ and $\phi(x)$.

The $F_{\mathrm{app}}(x)$ term in (5) defines the distribution of the *externally* applied loads. In the case of piezoelectric excitation, an equivalent external load distribution must be specified. The equivalent force is the force that would generate the same displacements as the piezoelectrically induced case. Fig. 1 illustrates the dependence of the equivalent external load for piezoelectric excitation on the deformation for the case of a fully electroded cantilever and a free-free beam. For both, the piezoelectric is in a state of compression. The magnitude of the equivalent external load is given by the block force of the piezoelectric. However, for the case of the cantilever, the equivalent load does not change sign, whereas for the free-free beam, each half of the beam possesses a different sign. This is further illustrated by solving (5) for these two cases:

$$F_{i\mathrm{Cant}} = \frac{-(e_{31}wV)}{L}\int_0^L \sin\left(\frac{\pi x}{2L}\right)\mathrm{d}x = \frac{-2}{\pi}(e_{31}wV) \tag{9}$$

$$F_{i\mathrm{FF}} = \frac{-(e_{31}wV)}{L}\int_0^{L/2}\cos\left(\frac{n\pi x}{L}\right)\mathrm{d}x + \frac{(e_{31}wV)}{L}\int_{L/2}^L\cos\left(\frac{n\pi x}{L}\right)\mathrm{d}x$$

$$= \frac{-2}{\pi}(e_{31}wV) \tag{10}$$

where $F_{i\mathrm{Cant}}$ and $F_{i\mathrm{FF}}$ are the amplitudes of modal forces for the fully electroded cantilever and free-free beams, respectively, e_{31} is the relevant piezoelectric stress constant, w is the width, and V is the applied voltage. The term $(e_{31}wV)$ is the magnitude of the equivalent external load and the mode shapes substituted into (5) are described in [39]. The modal forces happen to be identical for these cases, but only because the integral in (10) included the change in sign of the equivalent external load. If the distribution of the sign of the equivalent external load was not accounted for, the solution of (10) would yield zero. Therefore, the distribution of the sign of the equivalent external load must be determined from the static piezoelectric deformation of the structure subjected to the relevant mechanical boundary conditions.

It is clear from (5) that the piezoelectric equivalent external load must be specified to determine the modal
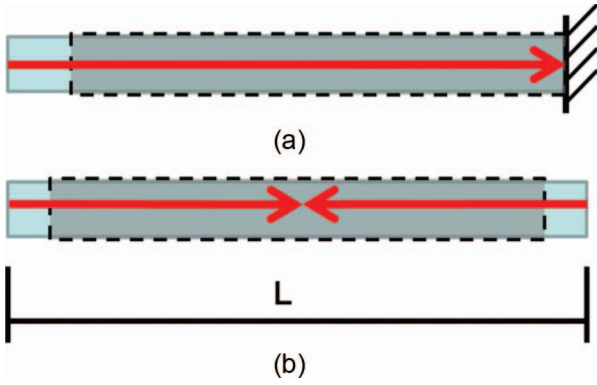
(a)

(b)

Fig. 1. (a) Illustration of fully electroded cantilever beam. The arrow indicates the equivalent external load under piezoelectric actuation and the dashed outline indicates the deformed beam shape. (b) Similar illustration for a fully electroded free-free beam.

Fig. 2. Element of an elastic medium being displaced by a one-dimensional longitudinal wave. The element of length $\mathrm{d}x$ experiences a displacement at the left face of u and a displacement at the right face of $u + \mathrm{d}u$. Under static deformation, both faces are acted upon by the traction forces F; under the dynamic conditions illustrated, the right face experiences an additional force of $\mathrm{d}F$.

force. Strictly speaking, the piezoelectrically induced static displacements in the structure must be known before the modal force can be determined. This can greatly complicate the task of ensuring that $F_{\mathrm{app}}(x)$ is proportional to the product of $m(x)$ and $\phi_j(x)$ to exclusively excite the jth mode, as previously discussed. Fortunately, the definition of $F_{\mathrm{app}}(x)$ is self-evident in the simple cases illustrated in Fig. 1, as well as for several other commonly used MEMS resonator designs.

B. Numerical Technique

As just illustrated, the traditional analytical approach features several challenges to determining electrode shapes in cases where the shape for the maximum modal force is not self-evident. Extending this to more complicated one-dimensional modes is difficult but extending the theory to higher dimensional modes, such as those existing in plates and discs, poses even greater complications. For example, the previous derivation relies upon the orthogonality property (1) of the one-dimensional mode shapes. However a general orthogonality principle that would apply to many higher dimensional cases does not exist [39]. In addition, to determine electrode-shapes in arbitrary cases, numerical techniques are either required or greatly facilitate the treatment of issues such as nontrivial geometries, modes not conveniently described by analytical models, deformation-coupling effects in asymmetric composites, anisotropic material properties, and the influence of non-optimal tether conditions on the mode shapes. An alternative to the traditional approach is to determine the local suitability of placing an electrode on the resonator. The electrode shapes are then ascertained from maps of this local determination of electrode placement.

To understand the local contribution of the piezoelectric to the overall modal response, consider Fig. 2. The figure illustrates a one-dimensional longitudinal wave propagating along the x direction of a medium of elastic modulus Y. The infinitesimal element, of length $\mathrm{d}x$, is strained by the tensile tractions F on both ends and experiences an
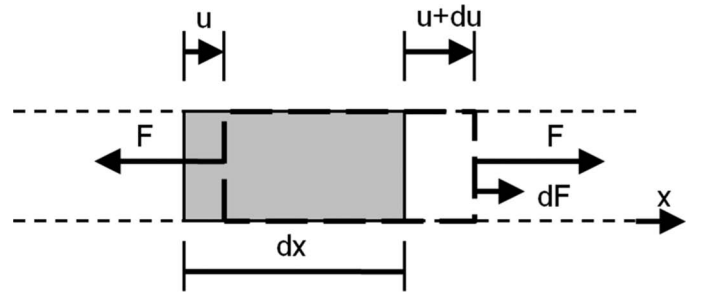
additional dynamic tensile force on the right face, $\mathrm{d}F$. The net force acting on the element is $\mathrm{d}F$ and is given by

$$\mathrm{d}F = \frac{\mathrm{d}\sigma}{\mathrm{d}x}\mathrm{d}x\mathrm{d}A = \frac{\mathrm{d}\varepsilon}{\mathrm{d}x}Y\mathrm{d}x\mathrm{d}A, \qquad (11)$$

where $\mathrm{d}A$ is the differential cross-sectional area, σ is the stress, and ε is the strain. We may define the strain distribution (12) and its derivative (13) in terms of the maximum strain, $\varepsilon_{\mathrm{max}}$, and the strain profile normalized to unity (term with bar), such that

$$\varepsilon(x) = \varepsilon_{\mathrm{max}}\overline{\varepsilon}(x) \qquad (12)$$

$$\frac{\mathrm{d}\varepsilon(x)}{\mathrm{d}x} = \varepsilon_{\mathrm{max}}\frac{\mathrm{d}\overline{\varepsilon}(x)}{\mathrm{d}x}. \qquad (13)$$

Solving (12) for $\varepsilon_{\mathrm{max}}$ and substituting the result into (13) yields

$$\frac{\mathrm{d}\varepsilon(x)}{\mathrm{d}x} = \varepsilon(x)\frac{1}{\overline{\varepsilon}(x)}\frac{\mathrm{d}\overline{\varepsilon}(x)}{\mathrm{d}x}. \qquad (14)$$

Substituting (14) into (11) illustrates that for normal mode vibrations, the local net dynamic force, dF, is a function of the magnitude of the local strain, $\varepsilon(x)$:

$$\mathrm{d}F = \frac{\mathrm{d}\sigma}{\mathrm{d}x}\mathrm{d}x\mathrm{d}A = \varepsilon(x)\left(Y\frac{1}{\overline{\varepsilon}(x)}\frac{\mathrm{d}\overline{\varepsilon}(x)}{\mathrm{d}x}\right)\mathrm{d}x\mathrm{d}A. \qquad (15)$$

This implies that maximizing the local strain leads to maximizing the local contribution to the modal force. Therefore, we may determine the local suitability of electrode placement by considering strain compatibility between the excited piezoelectric state and the desired mode at each location on the resonator. The mode is excited locally when the piezoelectrically induced stresses are consistent with the modal stresses; for example when the piezoelectric material is assumed to be in compression, it will excite regions of the resonator for modes where that location is also simultaneously in a state of compression.

In the case of attaching the piezoelectric drive transducer to the top surface of the resonator, we can consider

two adjacent differential volume elements, as illustrated in Fig. 3. One of these elements is associated with the excited piezoelectric and the other with the resonator vibrating in a specified mode shape (i.e., modal element). Assuming these elements are at the surface of the resonator, they are in a state of plane stress, which provides two nonzero in-plane normal stresses, σ_{m1} and σ_{m2}, and a nonzero shear stress τ_{12}. The maximum induced stresses in the piezoelectric element are those of the blocked forces of the piezoelectric volume element in the 1 and 2 directions. For the cases of lead zirconate titanate (PZT), AlN, and ZnO; the e_{31} and e_{32} piezoelectric stress constants are the same and hence the piezoelectric differential element is in a state of biaxial stress, with equal and invariant stress components σ_p. To compare the unequal number of stress components acting on the two differential volume elements and to ensure the solution for the electrode shape is invariant with respect to the choice of coordinate system, both elements are rotated into the principal plane of the modal element, see Fig. 4. This eliminates the shear stress τ_{12} in the modal element and obtains the invariant in-plane principal stresses in the modal element, σ_1 and σ_2. Because the piezoelectric element is under biaxial stress, its stress components are already principal values and are thus unaffected by the rotation. This permits the direct comparison of the stress components in the excited piezoelectric and the modal element to assess compatibility.

C. Implementation

Compatibility of the stress states must be considered for the same instant in time. For normal mode vibrations, all locations on the resonator experience synchronous displacements. We can, therefore, arbitrarily define the phase of the displacement of the excited piezoelectric volume element for all locations on the resonator such that the sign of piezoelectric stress components, σ_p, are taken as positive (tensile). This allows the instantaneous comparison of the stress components acting on the piezoelectric and modal elements. For example, at a particular location where both σ_1 and σ_2 are positive and σ_p has been assumed to be positive, the mode is locally excited. Furthermore, the sign of the differential modal force, the local contribution to total modal force, at this location is taken as positive. At a different location where both σ_1 and σ_2 are negative and σ_p has been assumed to be positive, the mode is locally inhibited. The sign of the differential modal force at this location is taken as negative. We can define a term, β, to represent the sign of the differential modal force in these locations.

$$\beta = \text{sign}(\sigma_1)\,\text{sign}(\sigma_p), \quad \text{where sign}(\sigma_1) = \text{sign}(\sigma_2) \quad (16)$$

$$\beta = 0, \quad \text{where sign}(\sigma_1) \neq \text{sign}(\sigma_2). \quad (17)$$

It is also possible for the two stress components, σ_1 and σ_2, to have different signs. For the case considered here ($e_{31} = e_{32}$), σ_1 and σ_p may have the same sign whereas
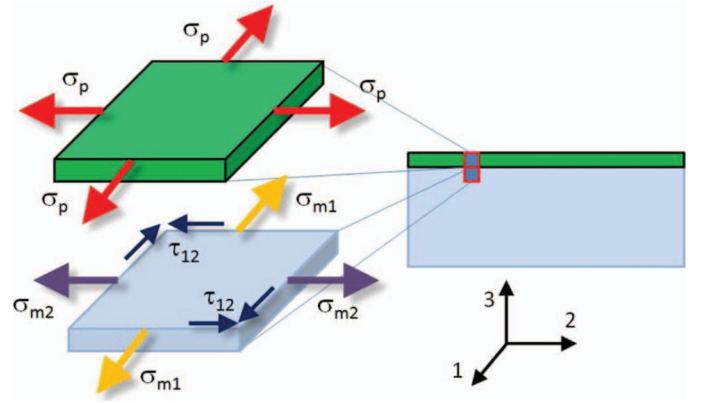

Fig. 3. Two adjacent differential volume elements taken from (right) a resonator consisting of a surface piezoelectric layer on a passive resonator layer: (top left) the excited piezoelectric material, (bottom left) an adjacent element (i.e., modal element) experiencing deformation dictated by a given mode shape. The traction forces illustrated correspond to a state of biaxial stress in the piezoelectric element and plane stress in the modal element.

σ_2 and σ_p may differ. At these locations, some degree of force cancellation occurs where the e_{31} piezoelectric stress constant may be locally exciting the mode whereas the e_{32} stress constant would be locally inhibiting the mode. At these locations, the sign of the differential modal force is determined by the degree of force cancellation and β is defined by (17).

The term β describes whether or not local force cancellation occurs between the induced stress components. In contrast, global force cancellation occurs if the entire excitation electrode covers regions of dissimilar β. The excitation electrode shape for a particular mode may be determined by finding those locations where the e_{31} and e_{32} piezoelectric stress constants both excite or inhibit the mode; the locations where local force cancellation does not occur. These are the locations where the two modal principal stress components have the same sign and the
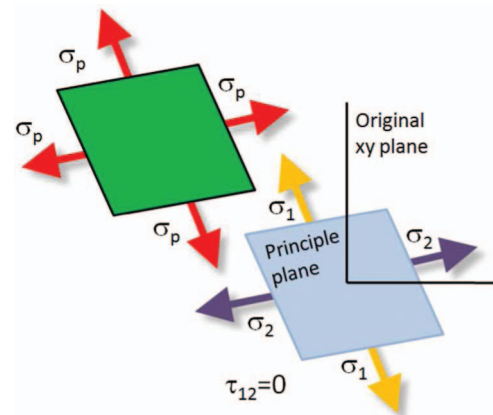

Fig. 4. Differential volume elements from Fig. 3 rotated into the principal plane of the modal element. The rotation eliminates the shear stress τ_{12} in the modal element and obtains the invariant in-plane principal stresses in the modal element, σ_1 and σ_2. This permits the direct comparison of the stress states in the two differential elements.

sign of the differential modal force is unambiguous and defined by β equal to either -1 or $+1$. The determination of the detection or sensing electrode consists of solving the constitutive equation for the direct piezoelectric effect locally for the differential of the induced charge, as given by

$$dq = (e_{31}x_x + e_{32}x_y + e_{33}x_z)dA \qquad (18)$$

where dq is the differential of the piezoelectrically induced charge, dA is the differential of the electrode area, the e_{ij} terms are the two transverse and one longitudinal piezoelectric stress constants, and the x_i terms are the x, y, and z strains. Whereas the derivation of the excitation electrode shape utilized a plane stress assumption, the use of three-dimensional strain in (18) is still valid and preserves generality with respect to the elastic equations of state. It should be noted that (18) can be rewritten in terms of effective film piezoelectric coefficients [40].

In summary, the technique determines excitation electrode shapes by determining the regions where local force cancellation does not occur; this ensures that global force cancellation does not occur either. The technique determines detection electrode shapes by determining the regions where global charge cancellation does not occur. Therefore, the technique determines optimal electrode shapes, with respect to global force and charge cancellation over the electroded surface, that permit the excitation and detection of the desired mode.

Because of the reciprocal nature of the piezoelectric direct and indirect effects, it is possible to use either technique to obtain one- or two-port electrode shapes. In this study however, both approaches have been used. Although the use of the direct effect is far simpler and provides information about the entire resonator surface, the derivation of (16) and (17) offers valuable theoretical insight into how the piezoelectrically induced forces relate to mode excitation.

III. Design

Execution of this technique consists of numerical modal analysis, Matlab (The MathWorks Inc., Natick, MA) data processing and scripted, automated CAD generation. To validate the technique, 61 different modes including plate, disc, ring, and beam geometries were designed and characterized. Table I lists the material properties and layer thicknesses and Table II lists the geometries utilized in the simulations. The composite resonator geometries were simulated in Ansys 12.0 (Ansys Inc., Canonsburg, PA) using 3-D 10-node tetrahedral structural (solid92) solid elements. For each of the four geometries, the modes between 1 and 200 MHz were simulated. The layers on top of the silicon were not patterned in the model. The effects of piezoelectricity on the modal results were neglected given the large ratio of silicon to PZT thickness (20:1). Following modal analysis the values and coordinates of the relative displacements, strains, and stresses were extracted on the top surface of the resonator. In Matlab, the finite-element analysis (FEA) mesh location referenced values were interpolated onto a denser regularly spaced grid to enhance the boundary definition between regions of dissimilar β. Direct use of the Ansys data resulted in coarse electrode shapes. β and the charge differential values from (16), (17), and (18) were determined at each location of the interpolated data set. Matlab was used to define coordinates of the boundaries between dissimilar β and the designer-defined charge-differential threshold locations. The resulting designs were down-selected based on favorable anchor loss and drive/sense electrode shapes. This selection process tended to favor particular modes and their harmonics, but the resulting 61 devices provide a diverse set of devices with which to investigate the theoretical design technique. Matlab code was then used to generate a CAD software script that automatically generated the selected electrode CAD geometries. Many of the designs feature asymmetric excitation and detection electrodes due, in part, to manufacturing limitations associated with electrode routing. In addition, many applications do not require symmetric devices; such as high-frequency electromechanical transformers [41]–[43]. The traces necessary to tie together isolated portions of the electrode shapes were routed through regions of low strain to minimize the mechanical loss contributions of the non-silicon materials in these locations.

TABLE I. Material Properties Used in the Simulations.

Layer	Thickness (μm)	Elastic modulus (GPa)	Density (kg/m^3)	Poisson's ratio				
BOX layer	0.2	60.2	2300	0.27				
Silicon (isotropic)	10	170*	2330	0.2152*				
Silicon dioxide	0.2	60.2	2300	0.27				
Platinum bottom electrode	0.1	141	18 000	0.3				
PZT	0.5	70	7800	0.3				
Platinum top electrode	0.1	141	18 000	0.3				
	$E_x = E_y$ (GPa)	E_z (GPa)	v_{yz}	v_{zx}	v_{xy}	$G_{yz} = G_{zx}$ (GPa)	G_{xy} (GPa)	
Silicon (orthotropic)	169	130	0.36	0.28	0.064	79.6	50h.9	

BOX = buried oxide; PZT = lead zirconate titanate.

*The isotropic silicon properties were used for design, and the orthotropic properties were utilized for characterization purposes.

TABLE II. CAD AND SIMULATION GEOMETRIES OF DEVICES.

	Length (µm)	Width (µm)	Outer diameter (µm)	Inner diameter (µm)
Disc	—	—	100	—
Plate	100	100	—	—
Ring	—	—	100	70
Beam	200	40	—	—

IV. FABRICATION PROCESS

The device fabrication is similar to the sequence outlined in [44] with the addition of significant improvements to address prior issues with yield and performance. The fabrication process flow for the PZT-on-silicon resonators is shown in Fig. 5. The devices are processed on a 100-mm silicon-on-insulator (SOI) wafer consisting of a 10-µm thick silicon device layer, 0.2-µm thick buried oxide layer, and a 500-µm thick handle layer of 1 to 30 Ω-cm resistivity. A 0.2-µm SiO_2 layer was deposited using plasma-enhanced chemical vapor deposition to provide a diffusion barrier between the silicon device layer and the bottom electrode layer. The bottom electrode consisted of a textured TiO_2 thin film and highly textured (111) Pt layer [45]. A 0.5-µm PZT layer with a Zr/Ti ratio of 52/48 was then deposited using a chemical solution deposition method with a crystallization temperature of 700°C [46] and subsequently coated with a 0.1-µm-thick top platinum electrode layer. The top electrode platinum and the PZT/bottom electrode were patterned via separate ion milling steps. Access to the bottom electrode was provided by a combination of ion-milling and wet-etch of the PZT using a combination of deionized water, hydrochloric acid, and hydrofluoric acid (2:1:0.02). A 0.02/0.73-µm titanium/gold bi-layer was then deposited via electron beam evaporation and patterned with liftoff to define the co-planar waveguide transmission line and necessary air-bridge contacts to Pt features. The resonator was then defined by anisotropic etching of the PZT, platinum, silicon dioxide, silicon device layer, and the buried oxide layer using a combination of ion-milling, reactive ion etching, and deep reactive ion etching. To ensure survival of the silicon layer of the resonators, a 0.15-µm layer of alumina was deposited via atomic layer deposition (ALD) to provide protection of the resonator while allowing release via undercutting of the handle wafer silicon using a subsequent XeF_2 etch. The advantages of this approach over the prior use of photoresist are outlined in [47]. The ALD alumina was then patterned with ion-milling. A planarizing thick photoresist layer process was developed to fill in the 10-µm-deep device silicon trenches to enable devices with gold air-bridges that spanned the trenches, facilitate subsequent photolithography, and to provide compatibility with wafer-level thin film encapsulation packaging processes [48]. To minimize the large parasitic capacitances associated with the high-dielectric-constant PZT and the large parasitic resistances associated with the thin platinum electrode layers, an organic sacrificial layer plus gold air-bridge process similar to that used in [49], was used. The photo definable organic (AZ 5200 resist, Clariant, Muttenz, Switzerland) was patterned and cured at 200°C. The 2-µm-thick gold air-bridge features were deposited via electron beam evaporation and patterned with liftoff. The air-bridges were then released using O_2 plasma dry etch to remove the hardened resist layer and the resonators were released from the handle silicon wafer with a XeF_2 dry silicon etch. An SEM image of a released PZT-on-silicon resonator is shown in Fig. 6.

V. RESULTS AND DISCUSSION

Multiple measurement and data analysis approaches were used to assess the electrode-shaping design technique to address the challenges, discussed in the introduction, associated with experimentally validating electrode-shaping. First, the simulation and experimental results of an example device are provided. Second, the simulation and experimental results for the 61 electrode-shaped resonator designs is presented and discussed. Third, the effective electromechanical coupling factors, k_{eff}, for each resonator design are compared with an ideal theoretical effective coupling factor to provide a relative measurement. Fourth, the difference in 50-Ω terminated insertion loss between designs intended for a given mode and designs not intended for that mode are compared. Finally, the correlation between electrode area effective coverage and insertion loss is verified to both assess the design technique and to permit the technique to predict potential spurious modes.

The fabricated, two port resonators were tested in a PA200 RF probe station (Suss MicroTec AG, Garching, Germany) at atmospheric pressure. The devices featured co-planar waveguide transmission lines (CPW) and ground-signal-ground (GSG) probes were used for testing. Full S-parameter matrices were extracted for each resonator using a ZVB vector network analyzer (Rohde & Schwarz, Munich, Germany). Two-port S-parameter calibration based on short, open, load, and through (SOLT) standards were performed on a GGB CSF-5 ceramic substrate. The devices were terminated to the internal 50-Ω impedance of the network analyzer. Wide- and narrow-band measurements were made of each resonator to characterize spurious modes and to obtain accurate effective coupling factors. Effective resonator coupling factors were extracted by transforming the measured two-port scattering parameters to ABCD parameters and solving for the one-port equivalent impedances. The k_{eff}^2 was then determined from the measured series and parallel resonant frequencies [10]. To improve poling of the PZT and provide consistent results, all devices were subjected to electric fields of 200 kV/cm for 5 min before testing.

A. Simulation and Experimental Results of Example Device

Fig. 7 illustrates a select example of an electrode-shaped PZT-on-silicon disc resonator operating in a high
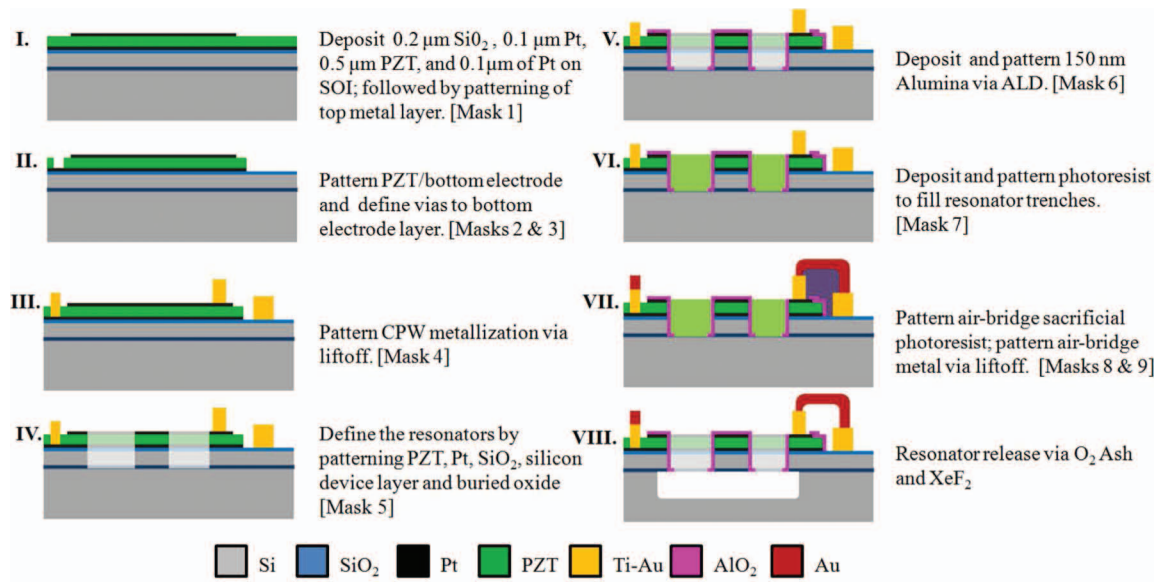
Fig. 5. Schematic view of the process flow used to fabricate lead zirconate titanate (PZT)-on-Si piezoelectric resonators.

order, out-of-plane, flexural mode. Fig. 7 features an optical micrograph of the fabricated device, an image of the corresponding FEA modeled mode shape, and the results of the electrode-shaping technique for the excitation and detection electrodes. The intended excitation port is on the left-side of the micrograph of Fig. 7(a). The mode shape data, Fig. 7(b), is plotted for the vector sum of displacements to highlight the nodal regions of the modes (in blue). (All references to color refer to the color images in the online version of this paper.) The red and blue regions of the excitation electrode shape, Fig. 7(c), correspond to the two possible excitation electrode locations defined by (16). These locations correspond to either tensile or compression regions of the modal analysis simulation and either location may be chosen. The green-colored regions indicate locations where the signs of the two principal modal stress components, σ_1 and σ_2, are dissimilar. These are the locations defined by (17) where local force cancellation occurs. The gradation in Fig. 7(d) illustrates the local intensity of the piezoelectrically induced charge [based on (18)] and displays the locations for the detection electrode. The red and blue graded locations correspond to either positive or negative charge regions of the modal analysis simulation and either may be chosen. The green-colored regions indicate locations where the piezoelectric charge differential (18) is close to zero. In both the excitation and detection cases, electrodes that overlap the two different regions will experience some degree of global force or charge cancellation, respectively.

Fig. 8 displays the frequency response of the measured forward transmission coefficient S_{21} of the device in Fig. 7; the dashed red line indicates the design resonant frequency for the intended mode. Fig. 9 plots the one-port equivalent impedance. This device exhibits 6.5 dB of 50-Ω terminated insertion loss at 68 MHz with a motional impedance of 82 Ω and a k_{eff}^2 of 0.67%. The proximity of

the lowest insertion loss mode to the design frequency in Fig. 8 and the prominence of the design mode in Fig. 9 suggest the electrode shape for this device is successfully exciting the desired mode.

B. Results for Beam, Plate, Disc, and Ring Resonators

Table III lists a summary of the experimental data obtained for the 61 electrode-shaped designs. The third column gives a brief description of the vibrational mode. In cases where the designation of the mode was ambiguous, the description is listed as unknown mode. The remainder of the table lists the predicted, measured, and error in resonant frequency; the 50-Ω terminated insertion loss, motional resistance, loaded quality factor, and the extracted one-port equivalent effective coupling factor. Figs. 10 and 11 provide images of the corresponding fabricated devices, the FEA modal results, and the predicted excitation and
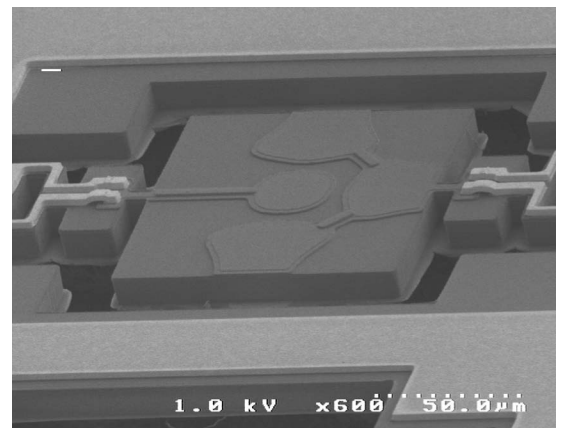

Fig. 6. Scanning electron microscopy image of a released lead zirconate titanate-on-silicon resonator.
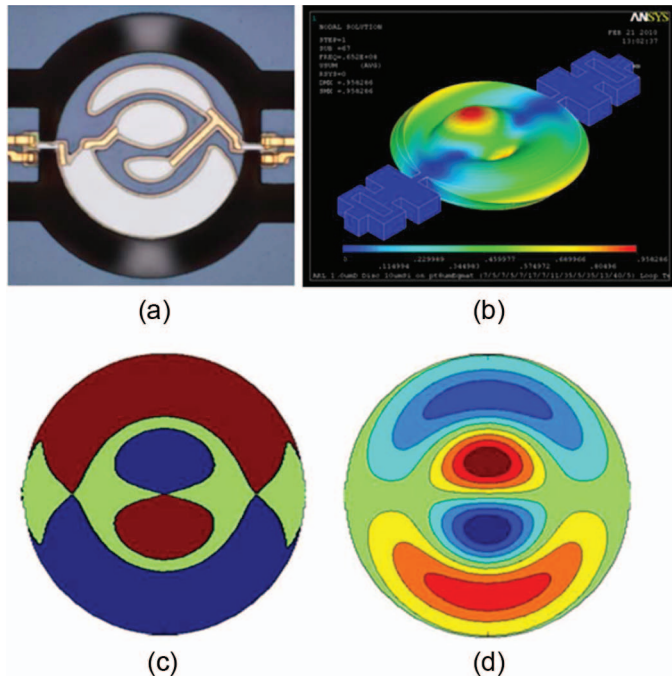
Fig. 7. Example disc resonator electrode-shaped for a high-order out-of-plane flexure mode illustrating: (a) optical micrograph of fabricated device, (b) finite element analysis (FEA) modal analysis plotting the vector sum of displacements (blue indicates zero displacement), (c) predicted excitation electrode shape, and (d) predicted detection electrode shape.

Fig. 8. Plot of the measured S_{21} transmission coefficient frequency response of the example device in Fig. 7.

detection electrode shapes. It is noteworthy that despite the independent theoretical derivation, the resultant excitation and detection electrode shapes in Figs. 10 and 11 share significant symmetry. This is expected because the excitation electrodes are defined by regions where local force cancellation does not occur and the detection electrodes are defined by regions where global charge cancellation does not occur.

The experimental set of devices features a diversity of mode types and their harmonics, including various out-of-plane flexure, face shear in plates, wineglass modes in discs and rings, and various contour-extensional modes. The beam designs #1 and #7 are the fundamental and third length-extensional modes. As seen in Fig. 11, the predicted excitation and detection shapes for this mode correspond to the electrode shapes commonly used for this mode in MEMS [4], [5], [24]. The predicted excitation shape for the harmonic device suggests force cancellation regions near the nodal locations and the ends of the device which experience a greater degree of extensional-flexural coupling. In contrast to the beam case, the second contour extensional mode in the plate (plate #13), possesses a more complex electrode shape. The technique predicts and the experimental results confirm the ability to excite and detect face shear modes in plates with PZT in a parallel plate electrode configuration. In contrast, the technique predicts that disc torsional modes are not capable of being excited because of the pure shear stress state of torsional modes.
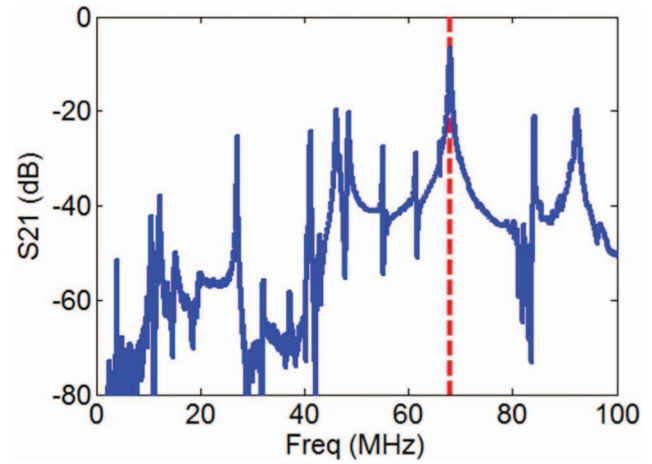
The simulations that provided the electrode shapes utilized the isotropic material properties for the silicon listed in Table I. However, to obtain the design frequencies for this analysis, the devices were simulated with the anisotropic material properties for silicon also listed in Table I. The properties used were the orthotropic properties defined in the frame of reference of the (100) device SOI wafer [50]. The discrepancies in the simulated frequencies were typically a few percent; however the frequencies of some modes differed by as much as 15%. Modest variations in the simulated mode shapes were only observed for very-high-frequency modes. The experimental resonant frequencies were initially determined by selecting prominent peaks in the scattering parameter data near the predicted frequencies. For nearly all of the data, the only prominent resonances in the one-port equivalent impedance frequency responses were these identified resonances. Table III illustrates that the measured and predicted resonant frequencies agree to within a few percent error.
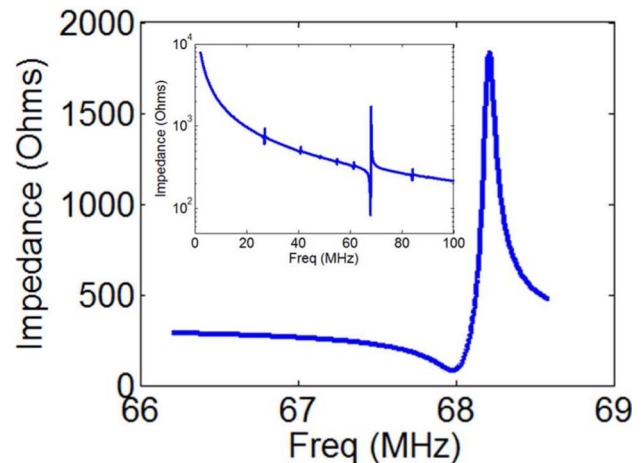

Fig. 9. Narrowband and (inset) wideband plots of the extracted one-port equivalent impedance frequency response of the example device in Fig. 7.

TABLE III: PERFORMANCE SUMMARY OF ELECTRODE-SHAPED RESONATORS.

Geometry	Design	Mode description	f_o, Theory (MHz)	f_o, Exp. (MHz)	Error (%)	IL (dB)	R_m (Ω)	Q_L (air)	k_{eff}^2 (%)
Plate	1	Z flexure, harmonic	12.31	12.76	−3.7	−28.6	1017	156	1.25
	2	Z flexure, harmonic	21.94	22.07	−0.6	−9.1	157	173	1.23
	3	Unknown mode	25.47	26.34	−3.4	−13.0	272	200	0.92
	4	Contour, face shear	25.50	26.40	−3.5	−31.1	1194	320	0.62
	5	Unknown mode	33.60	34.28	−2.0	−20.7	551	—	1.24
	6	Z flexure, harmonic	42.27	43.41	−2.7	−17.5	342	244	0.56
	7	Unknown mode	45.37	46.80	−3.1	−19.2	518	404	0.43
	8	Contour, unknown	49.33	48.46	1.8	−27.3	604	1346	0.14
	9	Unknown mode	50.18	51.00	−1.6	−14.5	314	425	0.42
	10	Unknown mode	62.17	63.68	−2.4	−20.6	499	346	0.36
	11	Unknown mode	60.35	62.09	−2.9	−24.5	528	324	0.46
	12	Unknown mode	63.34	63.79	−0.7	−16.5	358	313	0.53
	13	Contour-extensional, 2nd harmonic	81.21	77.84	4.2	−9.7	99	433	0.39
	14	Z flexure, harmonic	84.96	86.19	−1.5	−24.3	450	115	0.88
	15	Contour-face shear, harmonic	86.35	83.36	3.5	−17.0	256	268	0.57
	16	Unknown mode	108.07	110.28	−2.0	−23.8	289	158	0.91
Disc	1	Z flexure ($i = 1$, $j = 1$)	26.96	26.50	1.7	−5.8	87	221	1.17
	2	Contour (Wineglass)	33.49	32.64	2.5	−31.7	662	1166	0.16
	3	Contour, unknown	42.27	41.13	2.7	−23.5	429	332	0.54
	4	Z flexure, harmonic ($i = 2$, $j = 1$)	42.69	43.09	−0.9	−13.6	307	250	0.69
	5	Contour, Wineglass, harmonic	56.71	55.66	1.9	−15.2	285	994	0.21
	6	Z flexure, harmonic ($i = 3$, $j = 1$)	61.85	62.21	−0.6	−16.8	400	299	0.54
	7	Contour, unknown	61.42	59.77	2.7	−19.4	351	575	0.37
	8	Z flexure, harmonic ($i = 1$, $j = 2$)	68.05	67.99	0.1	−6.5	82	270	0.67
	9	Contour, Wineglass, harmonic	68.91	67.45	2.1	−18.7	354	1124	0.17
	10	Z flexure, harmonic ($i = 4$, $j = 1$)	79.50	80.72	−1.5	−20.7	482	374	0.41
	11	Z flexure, harmonic ($i = 2$, $j = 2$)	87.42	87.96	−0.6	−11.1	142	279	0.47
	12	Contour, Wineglass, harmonic	85.39	86.53	−1.3	−28.6	464	373	0.43
	13	Contour, unknown	89.13	84.57	5.1	−9.4	114	423	0.34
	14	Z flexure, harmonic ($i = 3$, $j = 2$)	109.14	109.72	−0.5	−22.1	334	398	0.31
	15	Z flexure, harmonic ($i = 1$, $j = 3$)	115.56	115.24	0.3	−11.2	127	238	0.60
	16	Z flexure, harmonic ($i = 5$, $j = 2$)	149.80	150.36	−0.4	−17.8	204	353	0.39
Ring	1	Contour, Wineglass	13.91	12.96	6.9	−43.6	3044	499	0.43
	2	Z flexure, harmonic	16.69	16.75	−0.4	−43.1	2137	200	0.88
	3	Z flexure, harmonic ($i = 1$, $j = 1$)	21.29	20.71	2.7	−29.6	935	137	0.86*
	4	Contour, Wineglass, harmonic	34.24	33.03	3.5	−36.0	1630	1033	0.20
	5	Z flexure, harmonic ($i = 2$, $j = 1$)	36.59	36.78	−0.5	−22.6	696	428	0.44
	6	Z flexure, harmonic ($i = 3$, $j = 1$)	54.68	54.42	0.5	−21.4	580	619	0.33
	7	Contour, Wineglass, harmonic	55.21	53.46	3.2	−37.7	1213	787	0.32
	8	Z flexure, harmonic ($i = 4$, $j = 1$)	90.52	85.04	6.1	−35.6	674	2181	0.08
	9	Z flexure, harmonic ($i = 1$, $j = 2$)	94.48	99.51	−5.3	−8.9	103	133	1.87*
	10	Contour, Wineglass, harmonic	94.48	96.54	−2.2	−25.9	376	403	0.64
	11	Z flexure, harmonic ($i = 2$, $j = 2$)	99.30	106.19	−6.9	−16.4	270	103	1.47*
	12	Z flexure, harmonic ($i = 1$, $j = 3$)	173.34	170.30	1.8	−16.9	161	164	0.84
	13	Unknown mode	188.32	181.92	3.4	−26.5	344	208	0.77
Beam	1	Contour, Length-extensional	19.10	18.92	0.9	−20.8	863	351	0.50
	2	Unknown mode	30.50	30.70	−0.7	−38.0	1440	770	0.30
	3	Z flexure, harmonic	35.20	35.34	−0.4	−18.6	534	431	0.32
	4	Contour, flexure-harmonic	38.73	37.44	3.3	−38.6	908	229	0.66
	5	Z flexure, asymmetric width flexure	45.26	46.09	−1.8	−35.5	349	161	0.75
	6	Unknown mode	48.10	47.65	0.9	−17.7	377	310	0.63
	7	Contour, length ext., 3rd harmonic	60.99	59.14	3.0	−16.1	265	247	0.71
	8	Contour, flexure, harmonic	55.53	60.99	−9.8	−29.8	501	1326	0.16
	9	Unknown mode	62.27	59.77	4.0	−40.4	880	729	0.23
	10	Unknown mode	66.23	65.81	0.6	−29.5	581	470	0.38
	11	Z flexure, harmonic	78.32	78.09	0.3	−20.6	495	476	0.33
	12	Unknown mode	80.46	78.33	2.7	−33.9	491	385	0.47
	13	Unknown mode	86.67	84.59	2.4	−21.1	290	798	0.22
	14	Unknown mode	92.88	95.58	−2.9	−29.9	612	498	0.35
	15	Z flexure, asym. width, harmonic	98.44	97.64	0.8	−33.1	314	235	0.71
	16	Contour, asym. width-extensional	100.05	99.85	0.2	−23.6	251	217	0.59

IL = insertion loss; i = number of nodal diameters; j = the number of nodal circles for disc and ring modes.

*k_{eff}^2 values have adjacent spurious modes.

Fig. 10. Design summary of electrode-shaped plate and disc resonators.

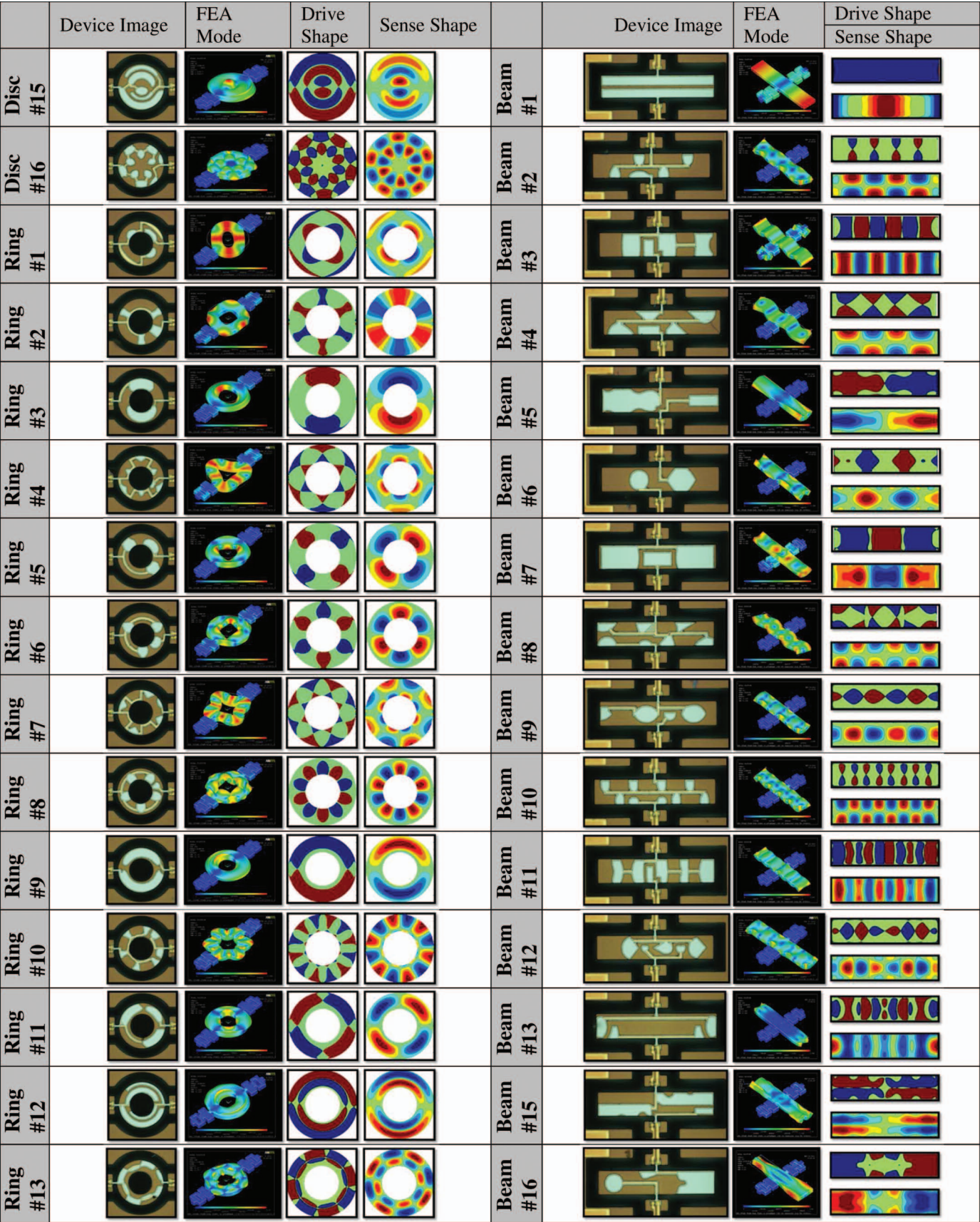|	Device Image	FEA Mode	Drive Shape	Sense Shape		Device Image	FEA Mode	Drive Shape / Sense Shape
Disc #15					Beam #1			
Disc #16					Beam #2			
Ring #1					Beam #3			
Ring #2					Beam #4			
Ring #3					Beam #5			
Ring #4					Beam #6			
Ring #5					Beam #7			
Ring #6					Beam #8			
Ring #7					Beam #9			
Ring #8					Beam #10			
Ring #9					Beam #11			
Ring #10					Beam #12			
Ring #11					Beam #13			
Ring #12					Beam #15			
Ring #13					Beam #16			

Fig. 11. Design summary of electrode-shaped disc, ring, and beam resonators.

The loaded quality factors for the devices were typically similar and in the low hundreds. Significant residual ALD alumina layers near the bottom edge of the resonator tethers are thought to have lowered the mechanical Qs of the devices; further process optimization is expected to address this in future devices. The few devices with Qs in excess of 1000 were, in almost all cases, contour modes. As contour modes are generally less sensitive to viscous damping, this suggests that air damping is a dominant loss mechanism for the non-contour modes. Therefore, in addition to process optimization, device operation in vacuum should further improve Q.

The 50-Ω terminated insertion losses of the devices range from 5.8 dB for an out-of-plane disc flexure mode (26.5 MHz) to 43.6 dB for the fundamental ring wineglass mode (13 MHz). The motional resistances of the devices range from 82 Ω for an out-of-plane harmonic disc flexure mode (see Fig. 7) to 3 kΩ for the fundamental ring wineglass mode (13 MHz). The lowest loss, resistance, and high effective coupling factor designs tended to be select out-of-plane flexure and contour extensional modes. The relative strength of high-frequency out-of-plane flexure modes over, for example, the contour disc and ring wineglass modes is likely due to the choice of silicon thickness. Increased silicon thickness can improve the effective resonator coupling factor for flexural modes but generally degrades the coupling factors for the contour modes. Consequently, higher performance of the wineglass modes is expected with thinner silicon thickness.

C. Analysis of Electromechanical Coupling

As a point of comparison to assess how well the electrode shapes perform, it is useful to compare the extracted k_{eff} values relative to an ideal value. There are multiple quasi-static coupling factors that are relevant in this study because of the diversity of modes explored. A single effective coupling factor, based on a quasi-static value, is utilized for the relative measure because of the difficulties in identifying the appropriate coupling factors for all of the devices. This does not provide a direct point of comparison for most of the devices, but provides a reasonable reference value. We will use the theoretical effective electromechanical coupling factor for the commonly utilized fully electroded beam resonator operating in the fundamental length extensional mode. This mode relies upon the k_{31} quasi-static coupling factor of the piezoelectric material [10]. For this mode, with low values of effective coupling, k_{eff}^2 and k_{31}^2 are related by the factor $8/\pi^2$ [51]. Furthermore, because k_{eff}^2 is fundamentally the ratio of the stored mechanical energy to the input electrical energy, the k_{eff}^2 of composite resonators are weighted by the mechanical-energy-storing non-piezoelectric layers. Therefore, the k_{eff}^2 of the composite length extensional mode resonator can be approximated by

$$k_{\text{eff}}^2 \approx \frac{8}{\pi^2} \frac{t_{\text{p}}}{t_{\text{si}}} \frac{Y_{\text{p}}}{Y_{\text{si}}} k_{31}^2, \qquad (19)$$

where t_{p} and t_{si} are the thicknesses of the piezoelectric and silicon layers, and Y_{p} and Y_{si} are the isotropic elastic modulus of the piezoelectric and silicon layers respectively. For 0.5-µm PZT ($d_{31,f} = -140$ pm/V and dielectric constant $\kappa_{33} \sim 500$ at 10 V bias [52]) on 10-µm silicon, the theoretical k_{eff}^2 of the composite length extensional mode resonator is 0.53%. The extracted k_{eff}^2 for this mode (Beam #1) is 0.50%, which differs from the theoretical value by only 6%. Fig. 12 plots the extracted effective electromechanical coupling factors of the resonators. The dashed red line indicates the reference coupling factor value. Many devices exceed this value; this is likely due to the modes exploitation of larger coupling factors such as k_{p}^2. In bulk PZT, k_{p}^2 can be nearly twice the value of k_{31}^2 [8]. The average effective coupling factor of the resonators is 0.54%. This value is nearly identical to the reference value, the theoretical maximum k_{eff}^2 of the composite length extensional mode beam resonator. The significance of this similarity is that the diversity of modes explored in this study, on average perform similarly to this arbitrarily chosen, but relevant, reference value. This suggests that the design technique predicted electrode shapes for these devices resulted in significant electromechanical coupling and successfully excited and detected the desired vibrational modes.

D. Analysis of Insertion Loss

Fig. 13 illustrates how the difference in 50-Ω terminated insertion loss between designs intended for a given mode and designs not intended for that mode were compared. Fig. 13 plots the measured S_{21} forward transmission frequency response of the two-port disc resonators near the resonant frequency of Disc #1 (listed in Table III). The highlighted region corresponds to a search window within $\pm 4\%$ of the design resonant frequency for Disc #1 (response is plotted in red). The red circles identify the peak S_{21} values within the search window for each disc resonator, $S_{21\text{window}}$; some of these values correspond to resonant peaks whereas other values are determined by electrical feed-through or the noise floor of the measurement. A measure of how well the Disc #1 electrode shape excites the intended mode is provided by ΔS_{21}; the difference between $S_{21\text{window}}$ of this design and the average of the $S_{21\text{window}}$ values for all of the other disc resonators not intended for this mode. ΔS_{21} was determined for each of the 61 resonators by comparing only like-geometries (i.e., plates were compared with plates, etc.). The $\pm 4\%$ search bandwidth was chosen as a compromise between a wide enough bandwidth to measure the intended vibrational mode and a narrow enough bandwidth to avoid comparing dissimilar modes.

Fig. 14 displays a stem plot of ΔS_{21} for each of the different electrode designs for each of the four different resonator geometries. Table IV summarizes the results of this analysis, including the number of designs of each geometry (N), minimum, maximum, and averages of ΔS_{21} for each
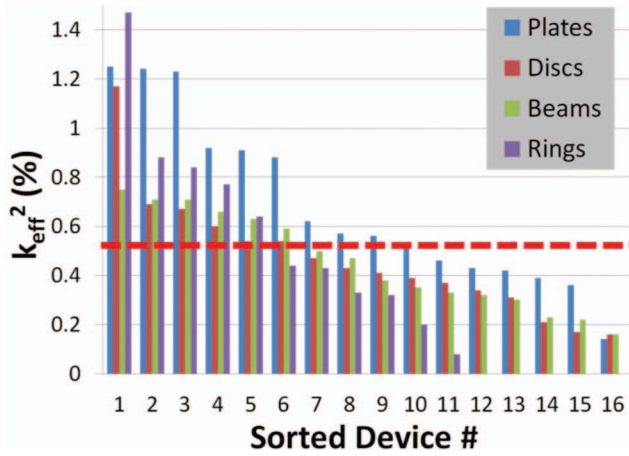
Fig. 12. The square of the extracted effective electromechanical coupling factors of the resonators. The dashed red line indicates the theoretical k_{eff}^2 of a fully electroded length-extensional mode resonator (0.53%) with the same composite structure as the measured devices.

Fig. 14. Stem plot of ΔS_{21} for each of the electrode-shaped designs. Each value represents the improvement in insertion loss of that mode relative to the average of the other designs within $\pm 4\%$ of the design frequency. Of the 61 designs, 95% showed a reduction in insertion loss (positive values).

geometry case. It should be noted that the average reduction in insertion loss for the four different geometry cases are significantly large and similar in value. The total average across the different geometries yields an improvement in S_{21} for the shaped designs of 14.6 dB and a maximum improvement of 44.3 dB. Of the 61 designs, 95% showed a reduction in insertion loss.

E. Electrode Area/Insertion Loss Correlation

It is expected that actual electrode designs that share a large effective percentage of area coverage with a given mode's predicted electrodes will result in excitation and detection of that particular mode. The correlation of electrode area effective coverage and insertion loss both

provides a means of assessing the design technique and enables the technique to identify potential spurious modes in the frequency response of a given design.

The net area overlap of each design's actual electrode that was common to the predicted electrode shape for the mode being characterized was determined. The net area overlap includes the actual layout geometry and the routing traces. Fig. 15 illustrates the area overlap for the excitation (drive) and detection (sense) electrodes of the Plate #3 CAD design with the Plate #1 modeled electrode shapes. Accounting for force cancellation, the net
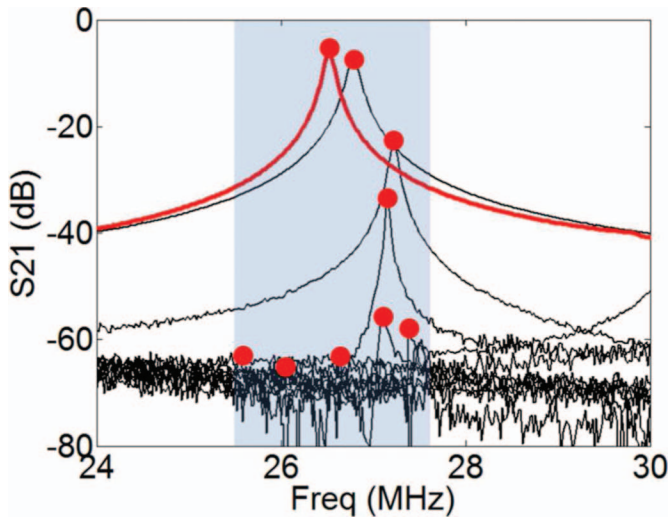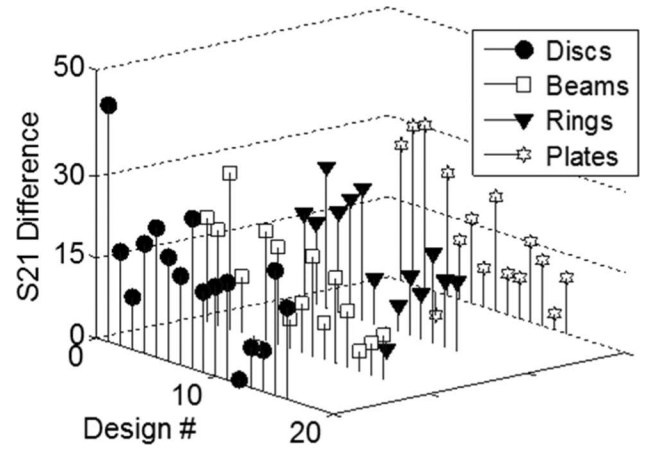

Fig. 13. The measured S_{21} forward transmission frequency responses of select two-port disc resonators near the resonant frequency of the Disc #1 design. The response of Disc #1 is plotted in red and the responses of other select disc resonators are plotted in black. The highlighted region corresponds to a search window within $\pm 4\%$ of the design resonant frequency for Disc #1. The red circles identify $S_{21window}$, the peak S_{21} values within the search window for each response.
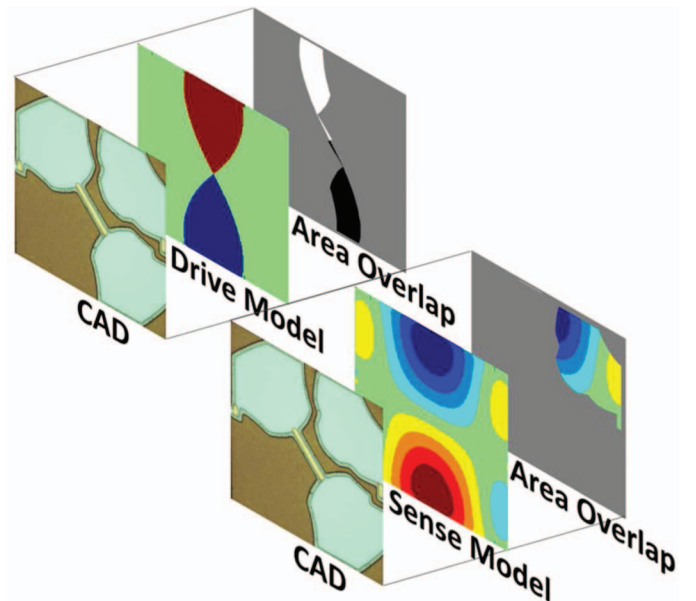

Fig. 15. Illustration of an example area overlap between actual as-fabricated device electrodes with predicted electrode shapes. CAD = Plate #3 design layout. Drive Model and Sense Model = predicted electrode shapes for the Plate #1 design. Area Overlap = resulting area overlap for the excitation (drive) and detection (sense) electrodes of the Plate #3 CAD design with the Plate #1 predicted electrode shapes.

TABLE IV. SUMMARY OF RESULTS FROM INSERTION LOSS DIFFERENCE ANALYSIS ILLUSTRATED IN FIG. 14.

Geometry	N	Insertion loss difference [dB]		
		Maximum	Minimum	Average
Plates	15	30.4	−4.2	14.3
Rings	16	26.2	−4.2	13.8
Beams	14	29.2	−1.9	12.3
Discs	16	44.3	1.0	18.0

N is the number of designs of each geometry type.

area overlap of the excitation electrode is the difference between the areas common to the two different force phase regions (white and black locations of the drive area overlap plot of Fig. 15). Accounting for charge cancellation, the net area overlap of the detection electrode is the difference between the areas common to the two different charge phase regions (see Fig. 15), linearly weighted by the intensity of the charge values. The net area overlap percentage of the excitation and detection electrodes is the percentage of the net area to the area of the larger of the two predicted phase electrode regions. For most devices, the net area overlap percentages were less than 100% because of difficulties in routing electrodes to utilize all desired electrode regions. For the two-port devices under analysis, the effective area overlap percentage is the product of the excitation and detection electrode net area overlap percentages.

Fig. 16 illustrates three examples, for the predicted electrode shapes of Disc #1, Ring #5, and Plate #1, of the correlation between effective area overlap percentage and $S_{21window}$. For a given mode's predicted electrode shapes (drive and sense model images of Fig. 15), the effective area overlap percentage was determined for each of the like-geometry CAD designs (CAD images of Fig. 15). The beam geometries were omitted because of a data process-

ing difficulty with determining the effective area overlap percentage of these devices. The Pearson correlation coefficients for these three cases are all above 90% (99%, 91%, 98%); suggesting significant correlation between these two parameters. Table V lists the Pearson correlation coefficients of the first five designs (lowest frequency) for the ring, plate, and disc geometries. Table V also lists the critical Pearson correlation coefficient values for the 99% level of statistical significance; coefficients greater than this value are statistically significant at the 99% level or better [53]. The data for 4 of 5 plate resonators, 5 of 5 ring resonators, and 4 of 5 disc resonators show statistical significance for correlation at this confidence level. This correlation suggests that the electrode shapes predicted by the technique can be used to predict spurious modes in the frequency response.

VI. CONCLUSION

A novel modeling and design technique has been demonstrated that permits the piezoelectric excitation and detection of vibrational modes, for the first time, in arbitrary cases of geometry and mode for those modes permitted to exist by the nonzero piezoelectric coefficients and electrode configuration. The technique determines optimal electrode shapes, with respect to force and charge cancellation over the electroded surface, that permit the excitation and detection of the desired mode. The technique was demonstrated in 61 different electrode designs in PZT thin film on silicon RF MEMS plate, beam, ring, and disc resonators for out-of-plane flexural and various contour modes up to 200 MHz. The average k_{eff}^2 for the designs was 0.54% and is nearly identical to the theoretical maximum value,
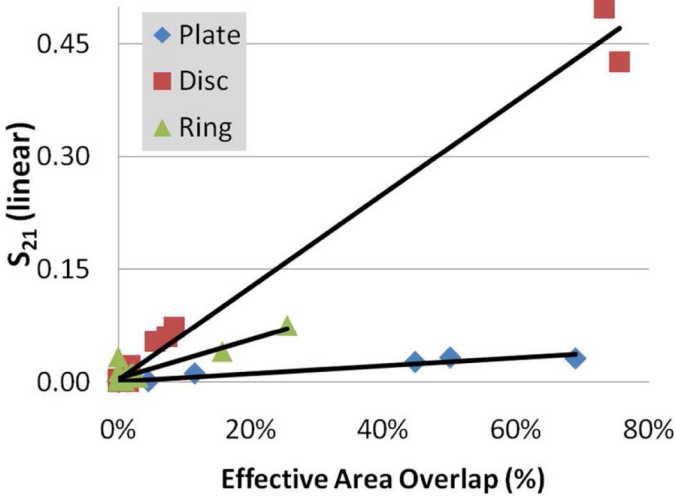

Fig. 16. Three device examples of the correlation between effective area overlap percentage and ΔS_{21} for ring, disc, and plate resonators. The majority of designs for each example have effective area overlap values near zero and consequently exhibit high insertion loss and suppression of these potential spurious modes.

TABLE V. PEARSON CORRELATION COEFFICIENTS OF THE FIRST FIVE DESIGNS (LOWEST FREQUENCY) FOR THE RING, PLATE, AND DISC GEOMETRIES.

	Plates	Rings	Discs
Design #1 (r)	0.98	0.74	0.99
Design #2 (r)	0.96	0.89	0.70
Design #3 (r)	0.98	0.90	0.04
Design #4 (r)	−0.22	0.95	0.77
Design #5 (r)	0.94	0.91	0.63
rcrit for 99%	0.64	0.62	0.62

The last row lists the critical Pearson correlation coefficient values (i.e., rcrit) for the 99% level of statistical significance. Note that all but two of the devices show statistical significance at better than the 99% level.

0.53%, for a fully electroded length-extensional mode beam resonator comprised of the same composite. Effective electromechanical coupling factors as high as 1.25%, motional resistances as low as 82 Ω, and 50-Ω terminated insertion loss as low as 5.8 dB were demonstrated at frequencies <100 MHz. The average improvement in S_{21} for the electrode-shaped designs was 14.6 dB with a maximum improvement of 44.3 dB, and 95% of the designs showed a reduction in insertion loss. Although the approach is broadly applicable to piezoelectric resonators, the specific implementation presented provides electrode-shapes for PZT, AlN, and ZnO transducers. Ongoing research is focused on extending the technique to achieve improved spurious mode suppression and obtaining an electromechanical and equivalent circuit model capable of predicting the contribution of all spurious modes to the frequency response of the device.

References

[1] R. Ruby and P. Merchant, "Micromachined thin film bulk acoustic resonators," in *Proc. Int. Frequency Control Symp.*, 1994. pp. 135–138.

[2] R. Ruby, P. Bradley, D. Clark, D. Feld, T. Jamneala, and W. Kun, "Acoustic FBAR for filters, duplexers and front end modules," in *Proc. MTT-S Int. Microwave Symp. Dig.*, 2004, vol. 2, pp. 931–934.

[3] C. T.-C. Nguyen, "MEMS technology for timing and frequency control," *IEEE Trans. Ultrason. Ferroelectr. Freq. Control*, vol. 54, no. 2, pp. 251–270, Feb. 2007.

[4] G. Piazza, P. J. Stephanou, and A. P. Pisano, "Single-chip multiple-frequency AlN MEMS filters based on contour-mode piezoelectric resonators," *J. Mictroelechromech. Syst.*, vol. 16, no. 2, pp. 319–328, Apr. 2007.

[5] R. H. Olsson, K. E. Wojciechowski, M. R. Tuck, and J. E. Stevens, "Multi-frequency aluminum nitride micro-filters for advanced RF communications," in *Government Microcircuit Applications and Critical Technology Conf.*, 2010, pp. 257–260.

[6] H. Fatemi, B. P. Harrington, H. Zeng, J. Carlisle, and R. Abdolvand, "50 Ω-terminated 900 MHz monolithic lateral-extensional piezoelectric filters on ultrananocrystalline diamond," in *Proc. IEEE Int. Conf. Micro Electro Mechanical Systems*, 2011, pp. 744–747.

[7] C. Zuo, N. Sinha, and G. Piazza, "Very high frequency channel-select MEMS filters based on self-coupled piezoelectric AlN contour-mode resonators," *Sens. Actuators A*, vol. 160, no. 1–2, pp. 132–140, May 2010.

[8] K. Uchino and J. Giniewicz, *Micromechatronics*. New York, NY: Marcel Dekker, 2003, pp. 242–254.

[9] G. K. Ho, R. Abdolvand, and F. Ayazi, "High order composite bulk acoustic resonators," in *Proc. 20th IEEE Int. Conf. Micro Electro Mechanical Systems*, 2007, pp. 791–794.

[10] *IEEE Standard on Piezoelectricity*, ANSI/IEEE Std. 176–1987, 1988.

[11] C.-K. Lee and F. C. Moon, "Modal sensors/actuators," *J. Appl. Mech.*, vol. 57, no. 2, pp. 434–441, 1990.

[12] M. I. Friswell, "On the design of modal actuators and sensors," *J. Sound Vibrat.*, vol. 241, no. 3, pp. 361–372, 2001.

[13] A. Preumont, A. Francois, P. De Man, and V. Piefort, "Spatial filters in structural control," *J. Sound Vibrat.*, vol. 265, pp. 61–79, 2003.

[14] W. Gawronski, "Modal actuators and sensors," *J. Sound Vibrat.*, vol. 229, no. 4, pp. 1013–1022, 2000.

[15] M. I. Friswell, "Partial and segmented modal sensors for beam structures," *J Vibrat. Control*, vol. 5, no. 4, pp. 619–637, 1999.

[16] R. Barboni, A. Mannini, and E. Fantini, "Optimal placement of PZT actuators for the control of beam dynamics," *Smart Mater. Struct.*, vol. 9, no. 1, pp. 110–120, 2000.

[17] H. Irschik, M. Krommer, A. K. Belyaev, and K. Schlacher, "Shaping of piezoelectric sensors/actuators for vibrations of slender beams:

[18] Coupled theory and inappropriate shape functions," *J. Intell. Mater. Syst. Struct.*, vol. 9, no. 7, pp. 546–554, 1999.

[18] M. I. Frecker, "Recent advances in optimization of smart structures and actuators," *J. Intell. Mater. Syst. Struct.*, vol. 14, no. 4–5, pp. 207–216, 2003.

[19] E. C. N. Silva and N. Kikuchi, "Design of piezoelectric transducers using topology optimization," *Smart Mater. Struct.*, vol. 8, no. 3, pp. 350–364, 1999.

[20] D. Tcherniak, "Topology optimization of resonating structures using SIMP method," *Int. J. Numer. Methods Eng.*, vol. 54, no. 11, pp. 1605–1622, 2002.

[21] M. Kögl and E. C. N. Silva, "Topology optimization of smart structures: Design of piezoelectric plate and shell actuators," *Smart Mater. Struct.*, vol. 14, no. 2, pp. 387–399, 2005.

[22] D. Tcherniak, "Topology optimization of resonating actuators," in *Proc. 12th Nordic Seminar on Computational Mechanics*, 1999, pp. 73–76.

[23] Z. Kang and L. Y. Tong, "Integrated optimization of material layout and control voltage for piezoelectric laminated plates," *J. Intell. Mater. Syst. Struct.*, vol. 19, no. 8, pp. 889–904, 2008.

[24] G. Piazza, P. J. Stephanou, and A. P. Pisano, "Piezoelectric aluminum nitride vibrating contour-mode MEMS resonators," *J. Microelectromech. Syst.*, vol. 15, no. 6, pp. 1406–1418, 2006.

[25] F. D. Bannon III, J. R. Clark, and C. T.-C. Nguyen, "High frequency micromechanical filters," *IEEE J. Solid-State Circuits*, vol. 35, no. 4, pp. 512–526, Apr. 2000.

[26] B. Piekarski, D. DeVoe, M. Dubey, R. Kaul, J. Conrad, and R. Zeto, "Surface micromachined piezoelectric resonant beam filters," *Sens. Actuators A*, vol. 91, no. 3, pp. 313–320, 2001.

[27] K. Wang, Y. Yu, A. C. Wong, and C. T.-C. Nguyen, "VHF free–free beam high-Q micromechanical resonators," in *Proc. IEEE 12th Annu. Int. Workshop on Micro Electro Mechanical Systems*, 1999, pp 453–8.

[28] S. Pourkamali, Z. Hao, and F. Ayazi, "VHF single crystal silicon elliptic bulk-mode capacitive disk resonators—Part II: Implementation and characterization," *J. Microelectromech. Syst.*, vol. 13, no. 6, pp. 1054–1062, 2004.

[29] J. Wang, J. E. Butler, T. Feygelson, and C. T.-C. Nguyen, "1.51-GHz polydiamond micromechanical disk resonator with impedance-mismatched isolating support," in *Proc. IEEE Int. MEMS Conf.*, 2004, pp. 641–644.

[30] S. A. Bhave, G. Di, R. Maboudian, and R. T. Howe, "Fully-differential poly-SiC Lame mode resonator and checkerboard filter," in *Proc. Int. Conf. Micro Electro Mechanical Systems*, 2005, pp. 223–226.

[31] A. Prak, M. Elwenspoek, and J. Fluitman, "Selective mode excitation and detection of micromachined resonators," *J. Microelectromech. Syst.*, vol. 1, no. 4, pp. 179–186, 1992.

[32] H. Tilmans, D. J. Untema, and J. Fluitman, "Single element excitation and detection of (micro-) mechanical resonators," in *Proc. Transducers '91*, 1991, pp. 533–537.

[33] A. Elka and I. Bucher, "Optimal electrode shaping for precise modal electromechanical filtering," *Struct. Multidiscip. Optim.*, vol. 38, no. 6, pp. 627–641, 2009.

[34] J. L. Sanchez-Rojas, J. Hernando, A. Donoso, J. C. Bellido, T. Manzaneque, A. Ababneh, H. Seidel, and U. Schmid, "Modal optimization and filtering in piezoelectric microplate resonators," *J. Micromech. Microeng.*, vol. 20, no. 5, art. no. 055027, 2010.

[35] A. Donoso and J. C. Bellido, "Systematic design of distributed piezoelectric modal sensors/actuators for rectangular plates by optimizing the polarization profile," *Struct. Multidiscip. Optim.*, vol. 38, no. 4, pp. 347–356, 2009.

[36] J. He and Z.-F. Fu, *Modal Analysis*. Woburn, MA: Butterworth-Heinemann, 2001.

[37] L. Meirovitch, *Fundamentals of Vibrations*. New York, NY: McGraw-Hill, 2001.

[38] S. S. Rao, *Mechanical Vibrations*. Reading, MA: Addison-Wesley, 1995.

[39] R. D. Blevins, *Formulas for Natural Frequency and Mode Shape*. Malabar, FL: Krieger, 1984, pp. 236.

[40] M.-A. Dubois and P. Muralt, "Measurement of the effective transverse piezoelectric coefficient $e_{31,f}$ of AlN and $Pb(Zr_x, Ti_{1-x})O_3$ thin films," *Sens. Actuators A*, vol. 77, no. 2, pp. 106–112, Oct. 1999.

[41] S. Bedair, J. Pulskamp, B. Morgan, and R. Polcawich, "Performance model of electrode tailored thin film piezoelectric transformers for

high frequency switched mode power supplies," in *Power MEMS 2009*, pp. 435–438.

[42] R. H. Olsson III, K. E. Wojciechowski, M. R. Tuck, and J. E. Stevens, "Microresonant impedance transformers," in *Proc. IEEE Int. Ultrasonics Symp.*, 2009, pp. 2153–2157.

[43] P. Laoratanakul, A. V. Carazo, P. Bouchilloux, and K. Uchino, "Unipoled disk-type piezoelectric transformers," *Jpn. J. Appl. Phys.*, vol. 41, pp. 1446–1450, Mar. 2002.

[44] H. Chandrahalim, S. A. Bhave, R. Polcawich, J. Pulskamp, D. Judy, R. Kaul, and M. Dubey, "Influence of silicon on quality factor, motional impedance, and tuning range of PZT-transduced resonators," in *Solid State Sensor, Actuator and Microsystems Workshop*, 2008, pp. 360–363.

[45] D. M. Potrepka, G. R. Fox, L. M. Sanchez, and R. G. Polcawich, "Pt/TiO$_2$ growth templates for enhanced PZT films and MEMS devices," in *Materials Research Society Online Proc. Library*, vol. 1299, art. no. mrsf10-1299-s04-02, 2010.

[46] L. M. Sanchez, D. M. Potrepka, G. R. Fox, I. Takeuchi, and R. G. Polcawich, "Improving PZT thin film texture through Pt metallization and seed layers," in *Materials Research Society Online Proc. Library*, vol. 1299, art. no. mrsf10-1299-s04-09, 2010.

[47] G. L. Smith, R. G. Polcawich, J. S. Pulskamp, T. Waggoner, and J. F. Conley, Jr., "Atomic layer deposited alumina for use as an etch barrier against xenon difluoride etching," in *Solid State Sensor, Actuator and Microsystems Workshop*, 2010, pp. 194–198.

[48] K. D. Leedy, R. E. Strawser, R. Cortez, and J. L. Ebel, "Thin-film encapsulated RF MEMS switches," *J. Microelectromech. Syst.*, vol. 16, no. 2, pp. 304–309, Apr. 2007.

[49] R. G. Polcawich, D. Judy, J. S. Pulskamp, S. Trolier-McKinstry, and M. Dubey, "Advances in piezoelectrically actuated RF MEMS switches and phase shifters," in *IEEE/MTT-S Int.Microwave Symp.*, 2007, pp. 2083–2086.

[50] M. A. Hopcroft, W. D. Nix, and T. W. Kenny, "What is the Young's modulus of silicon?" *J. Microelectromech. Syst.*, vol. 19, no. 2, pp. 229–238, Apr. 2010.

[51] "IRE standards on piezoelectric crystals: Determination of the elastic, piezoelectric, and dielectric constants—The electromechanical coupling factor," *Proc. IRE*, vol. 46, no. 4, pp. 764–778, Apr. 1958.

[52] R. G. Polcawich and J. S. Pulskamp, "Additive processes for piezoelectric materials: Piezoelectric MEMS," in *MEMS Materials and Processes Handbook*, 1st ed., R. Ghodssi and P. Lin, Ed. New York, NY: Springer, 2011, pp. 273–344.

[53] N. M. Downie and R. W. Heath, *Basic Statistical Methods.* New York, NY: Harper & Row, 1959, pp. 154–156.

Jeffrey S. Pulskamp is a MEMS Design and Mechanical Engineer in the Micro & Nano Materials & Devices Branch of the US Army Research Laboratory (ARL), Adelphi, MD. He received a B.S. degree in mechanical engineering from the University of Maryland, College Park, MD, in 2000. His current research interests include RF MEMS resonators and switches, electro-mechanical design and modeling of MEMS, and millimeter-scale robotics. He currently holds 8 patents related to piezoelectric MEMS devices and has an additional 5 patents pending and has authored one book chapter on the design and fabrication of piezoelectric MEMS devices.

Sarah S. Bedair received the B.S. degree in applied sciences & computer engineering from the University of North Carolina–Chapel Hill (2002, Magna Cum Laude with Highest Distinction). She also received her Ph.D. and M.S. degrees in electrical & computer engineering from the Carnegie Mellon University, in 2004 and 2008, respectively; her thesis work focused on CMOS MEMS-based chemical gravimetric sensors and mechanical oscillators.

Dr. Bedair spent one year (August 2008–June 2009) as an Oak Ridge Associated University Postdoctoral Fellow at the U.S Army Research Laboratory (ARL) in Adelphi, MD. She has been a staff researcher in the Power Components Branch at ARL since June 2009. Her research is on the modeling and fabrication of MEMS-based power devices, specifically for single-chip-scale power conversion and RF electronics. She has contributed to more than 25 research publications and is co-inventor on 4 patent applications or invention disclosures awaiting patent submission. She is also a member of IEEE.

Dr. Bedair has received fellowships and awards for excellence in academics and research. These include the Phillip and Marsha Dowd-Institute for Complex Engineered Systems Fellowship and the James D. Crawford Award at UNC–Chapel Hill. She also received the 2010 Excellence in Federal Career–Technical & Scientific Rookie of the Year Award and the 2009 ARL Research and Development Achievement Award.

Ronald G. Polcawich is a staff researcher in the Micro & Nano Materials & Devices Branch of US Army Research Laboratory (ARL), Adelphi, MD. He received a B.S. degree in materials science and engineering from Carnegie Mellon University in 1997, an M.S. degree in materials from Penn State University in 1999, and a Ph.D. degree in materials science and engineering from Penn State University in 2007. He is currently the team lead for the RF MEMS and Millimeter-Scale Robotics programs at ARL. The current research programs include switches and phase shifters for phased array antennas, tunable MEMS resonators/filters for secure communication, and mobile unattended sensor platforms. His research activities include materials processing of PZT thin films, MEMS fabrication, piezoelectric MEMS, RF components, MEMS actuators, and millimeter-scale robotics. He currently holds 5 patents, has 8 patent applications pending review, and has authored more than 30 journal articles and one book chapter on fabrication and design of piezoelectric MEMS devices. Dr. Polcawich is a member of IEEE.

Gabriel L. Smith received his B.S. and M.S. degrees in mechanical engineering from the University of Maryland, College Park, in 1999 and 2002, respectively. He has worked in MEMS design for the past 15 years with the U.S. Naval Surface Warfare Systems, U.S. Army Armaments Research Development and Engineering Center, and U.S. Army Research Laboratory. He has developed MEMS devices for safe and arm devices in torpedoes and gun-launched munitions, piezoelectric sensors and actuators for millimeter-scale robotic systems, and piezoelectric traveling wave ultrasonic motors. He has also fielded MEMS impact switches in Army systems for target and launch detection. He currently holds six US patents with three patents pending and has authored nine journal and conference papers on MEMS devices.

Joel Martin is a fabrication technician in the Micro & Nano Materials & Devices Branch of US Army Research Laboratory (ARL), Adelphi, MD. He received advanced electronics training in submarine communications while serving in the U.S. Navy from 1984 to 1996. He is currently the lead technician for photolithography and sputter deposition for the RF MEMS and Millimeter-Scale Robotics programs at ARL. He received the ARL Award for Technician in 2010 for process development and fabrication expertise in support of the piezoelectric-based miroelectromechanical systems (MEMS) program. Over the past five years, Mr. Martin has been responsible for the fabrica-

tion of more than 1000 device and test wafers covering everything from RF switches to resonators/filters, mechanical logic, phase shifters, actuators for bio-inspired microflight, and ultrasonic traveling wave motors.

Brian Power is an Engineering Technician in the Micro & Nano Materials & Devices Branch of US Army Research Laboratory (ARL), Adelphi, MD. He is currently the lead technician for ion-milling and metal evaporations for the RF MEMS and Millimeter-Scale Robotics programs at ARL. He received the ARL Award for Technician in 2010 for his expertise in the fabrication of piezoelectric-based MEMS programs. Over the past five years, Mr. Power has been responsible for the fabrication of more than 1000 device and test wafers covering everything from RF switches to resonators/filters, mechanical logic, phase shifters, actuators for bio-inspired microflight, and ultrasonic traveling wave motors.

Sunil A. Bhave (S'99–M'04–SM'10) received the B.S. and Ph.D. degrees in electrical engineering and computer sciences from the University of California, Berkeley, in 1998 and 2004, respectively. Since October 2004, he has been with Cornell University, Ithaca, NY, where he is currently an Associate Professor with the School of Electrical and Computer Engineering. His research interests include microelectromechanical resonators for radio front ends, merged complementary metal–oxide–semiconductor and nanoelectromechanical systems (NEMS) for low-power computation, inertial and acoustic sensors, and hybrid photonic NEMS and magnetic NEMS for low-phase-noise microwave oscillators.

Dr. Bhave was a recipient of the National Science Foundation Early CAREER Development Award in 2007 and the Defense Advanced Research Projects Agency Young Faculty Award in 2008. Along with his students, he has been awarded the Roger A. Hakan Best Paper Award at International Electron Devices Meeting 2007 and is the winner of the Student Paper Competition at the 2009 IEEE International Ultrasonics Symposium.